RSC Advances

PAPER

View Article Online
View Journal | View Issue

Cite this: *RSC Adv.*, 2022, **12**, 6676

Enhanced photocatalytic activity of TiO_2/UiO-67 under visible-light for aflatoxin B1 degradation†

Jia Zhang, Xintong Gao, Wenbo Guo, Zengnan Wu, Yilin Yin and Zenghe Li *

Received 30th December 2021
Accepted 16th February 2022

DOI: 10.1039/d1ra09441f

rsc.li/rsc-advances

TiO_2 has great potential in photocatalytic degradation of organic pollutants, but poor visible light response and low separation efficiency of photogenerated electron–hole pairs limit its wide applications. In this study, we have successfully prepared TiO_2/UiO-67 photocatalyst through an *in situ* solvothermal method. The degradation rate of aflatoxin B1 (AFB1) is 98.9% in only 80 min, which is superior to the commercial P25, commercial TiO_2 and most of reported photocatalysts under visible light irradiation. In addition, the TiO_2/UiO-67 photocatalyst showed excellent recyclability. We demonstrated that the enhanced photocatalytic mechanism was owing to the heterojunction between TiO_2 and UiO-67, which enhanced effectively the separation photogenerated charge carriers and visible light response. The free radical trapping tests demonstrated that superoxide radicals ($^{\bullet}O_2^-$), holes (h^+) and hydroxyl radicals ($^{\bullet}OH$) were the main active species and then oxidized AFB1 to some small molecules.

1. Introduction

Environment and energy are crucial topics in human sustainable development. Most environmental pollutants are harmful to the environment, seriously affect ecosystems and threaten human health. In particular, aflatoxins mainly generated from agricultural products have highly mutagenic and teratogenic effects.[1–4] Therefore, we must pay more attention to aflatoxins with high toxicity and chemical stability. However, there are few green and mild ways to degrade aflatoxins.[5] Photocatalysis is considered as an effective strategy for degrading chemical pollutants from the environment.[6,7] Under sunlight irradiation, the valence band (VB) electrons of the semiconductor are excited to the conduction band (CB), so that the VB is occupied by holes (h^+), while the electrons accumulate in the CB of the semiconductor. Furthermore, the photogenerated electrons in the CB react with oxygen to generate superoxide radicals ($^{\bullet}O_2^-$), and holes in the VB react with dissolved O_2 or H_2O/OH^- in water to generate hydroxyl radicals ($^{\bullet}OH$). These reactive oxygen species then reacted with the targeted species that adsorbs on the surface of the catalyst promoting its degradation.[8–12]

Lots of studies about oxide semiconductor photocatalysts have been focused on anatase titanium dioxide (TiO_2) because of its chemical stability, low cost, non-toxicity, and low environmental impacts.[13] Nevertheless, photocatalytic effect is refrained due to its inherent defects such as a single-response only to UV light and low separation efficiency of photogenerated electron–hole pairs.[14] There are effective technical strategies including defect engineering, surface and interface engineering and heterojunction for improving photocatalysis efficiency.[15–17] Heterojunction, one of the best ways to improve photocatalytic activity, can reduce electron–hole recombination and improve light absorption range through the combination of two different semiconductors with matched energy band structures.[18–21]

Metal organic frameworks (MOFs) have attracted extension because of their large specific surface area, large pore volume, and the ability to introduce different electron densities by adjusting the length of the ligand.[22–24] In addition, the electrons of some MOFs can be transferred from HOMO to LOMO, and further generate photo-generated electrons and holes under the excitation of light, which can be used as photocatalysts.[25–27] Based on these advantages, MOFs with appropriate band gaps can be used to construct various types of heterojunctions with TiO_2 to enhance photocatalytic performance. There have reported that MOFs can be used to construct heterojunction with TiO_2 to improve photocatalysis activity in previous study.[28,29] For instance, Zhang *et al.* fabricated TiO_2@UiO-66 composite with high photocatalysis degradation performance of VOCs due to TiO_2 and UiO-66 have matched energy band structures and effective separation of photogenerated charge carriers.[30] Zhang *et al.* synthesized TiO_2/mag-101(Cr) combined the advantages of TiO_2, MOFs and Fe_3O_4 to improve photocatalysis degradation efficiency of organic pollutants.[31] In recent years, UiO-67, one of the Zr-MOFs, has large surface area, good photocatalysis activity and lower bandgap (3.14 eV),[32] which has better light response than TiO_2.[33] Therefore, designing TiO_2/UiO-67 heterostructures is a feasible approach for improving the photocatalytic activities of TiO_2.

Key Laboratory of Environmentally Harmful Chemical Analysis, College of Chemistry, Beijing University of Chemical Technology, Beijing, 100029, China. E-mail: lizh@mail.buct.edu.cn

† Electronic supplementary information (ESI) available. See DOI: 10.1039/d1ra09441f

In this work, we first synthesized TiO_2/UiO-67 composites that can efficiently degrade AFB1 by *in situ* solvothermal method. The photocatalysis experiment showed that TiO_2/UiO-67 composites have good photocatalytic degradation effect and stability under visible light. The structure, morphology, and surface chemical compositions of the TiO_2/UiO-67 heterostructure (T-10%U) were discussed in detail. Combining the results of photoelectrochemical properties and spectroscopy data, we concluded that the improved photocatalytic performance of the TiO_2/UiO-67 composites is mainly due to TiO_2 and UiO-67 forms a heterojunction. In addition, free radical capture experiments can further prove the variety of main active species produced in the photocatalytic process.

2. Experimental section

2.1. Chemicals

All chemical reagents were analytical grade without purification treatment. For high-performance liquid chromatography (HPLC) analysis, methanol (HPLC grade) was purchased from Thermo Fisher Scientific. Tertiary butyl alcohol (TBA, $C_4H_{10}O$) was purchased from Tianjin Fuchen Chemical Reagents Factory. Titanium oxide (anatase), titanium butoxide, ethylene diamine tetraacetic acid (EDTA) were purchased from Aladdin (Shanghai). *N*,*N*-Dimethylformamide (DMF), ethanol and acetic acid were purchased from Tianjin Damao Chemical Reagents Factory (Tianjin China). Na_2SO_4, 1,4-benzoquinone (BQ, $C_6H_4O_2$) were obtained from Tianjin Guangfu Fine Chemical Research Institute. Biphenyl-4,4′-dicarboxylic acid, zirconium(IV) chloride, Nafion perfluorinated resin solution (5 wt% in mixture of lower aliphatic alcohols and water, contains 45% water) were received from Shanghai Macklin Biochemical Co., Ltd. Deionized water was used in all experiments.

2.2. Preparation of catalysts

2.2.1. UiO-67 preparation. UiO-67 was prepared as following preliminary research: typically, 270 mg biphenyl-4,4′-dicarboxylic acid and 201 mg of zirconium(IV) chloride were well dispersed in 45 mL DMF. Then 4.2 mL ethanoic acid was added to the above mixture to form homogeneous solutions *via* a continuous stirring process for 10 min. The mixture was kept in a Teflon-lined stainless-steel autoclave, which was heated to 120 °C for 24 h. Finally, the samples were washed with DMF three times and the DMF in the pores of UiO-67 was removed further by heat treatment at 120 °C for 12 h.[34]

2.2.2. Preparation of TiO_2/UiO-67 heterojunctions and TiO_2. TiO_2/UiO-67 photocatalyst (named as T-*X*U, where *X* is the mass ration of the UiO-67 (X = 2.5%, 10%, 10%, 30%) with respect to tetrabutyl titanate) was synthesized by a simple *in situ* solvothermal method according to previous references.[31] In the prepared process, 0.2 mL tetrabutyl titanate, 30 mL ethanol and 3 mL acetic acid were mixed to form transparent homogeneous solutions. Then different mass ratio UiO-67 was dispersed to the above solutions and stirred for 30 min. Then the mixture was transformed into a Teflon-lined stainless steel autoclave, which was heated to 220 °C for 4 h. Subsequently, the precipitates were collected by centrifugation and washed with ethanol to neutral. And then the products were dried at 60 °C for 12 h. The fabrication of pure TiO_2 is consistent with the above method without UiO-67.

2.3. Characterization

X-ray diffraction (XRD, Ultima IV) was used to characterized the crystal structure of materials. Crystal morphologies and microstructure of synthesized materials can be analysed by SEM (Supra 55) and TEM (JEM-F200) equipped with energy dispersive X-ray. The chemical composition and valence state of the sample surface was characterized by Thermo Scientific X-ray photoelectron spectroscopy (XPS) with Al Kα irradiation. Fourier transform infrared (FTIR) (Thermo Fisher Nicolet 6700) was used to confirm active groups of the sample. UV-vis diffuse reflectance spectra (DRS) were monitored by UV-3600 UV Spectrometer (SHIMADZU) in the 200–800 nm wavelength range. Photoluminescence spectra (PL) was obtained by using HITACHI F-7000 with the excitation light at 300 nm.

2.4. Photocatalytic measurement

The photocatalytic performance of the composite was carried under a 300 W high-pressure xenon lamp with a UV-cutoff filter (λ > 420 nm, CEL-HXF300, Beijing Zhongjiao Jinyuan Technology Co., Ltd). The reaction was carried out with 10 mg photocatalyst and 100 mL AFB1 aqueous solution (0.5 μg mL^{-1}). The mixture was stirred in atmosphere and kept in dark for 30 min in order to reach the equilibrium of adsorption–desorption. After visible light irradiation, the supernatant (1 mL) was filtrated with a 0.22 μm filter and analyzed by a HPLC (Beijing Mingnike P2000) with C18 column (length of 254 mm, inner diameter of 4.6 μm, diameter of 5 μm, Leena) and an UV-visible detector. The detection condition of HPLC: 65% methanol aqueous solution was used as the mobile phase; the flow rate is set to 1.0 mL min^{-1}. The detection wavelength was set at 365 nm and 20 μL sample was injected for each analysis. We calculated the AFB1 removal efficiency according to the formula:

$$\text{AFB1 removal efficiency} = (1 - CV/C_0V_0) \times 100\%$$

here, C_0 (μg mL^{-1}) and V_0 (mL) were the initial AFB1 concentration and volume respectively; c (μg mL^{-1}) and V (mL) represented the AFB1 concentration and volume after degradation.

2.5. Photoelectrochemical measurement

The photoelectrochemical measurement of photocatalysts were performed on CHI 660E electrochemical system (CH Instruments Inc., Shanghai) with a traditional three electrode cell (a saturated Ag/AgCl electrode, a Pt counter electrode and a working electrode). We prepared working electrode as follows: 5 mg of catalyst was dispersed in 800 μL ethanol, 200 μL deionized water and 40 μL Nafion solution were mixed to form a homogeneous solution with ultrasonic treatment, and then the mixture is dripped onto the FTO (1 cm × 3 cm) saved as working electrode. The photocurrent was implemented under a 300 W xenon lamp (λ > 420 nm) irradiation with 30 mL Na_2SO_4

aqueous solution (1 M). Electrochemical impedance spectroscopy (EIS) measurement is performed in the frequency ranged of 1–10^5 Hz with 5 mV sinusoidal alternating current. Photocurrent measurements and Mott–Schottky experiments were conducted with voltage ranged from −0.5 to 0.5 V, according to previous reports.[35,36]

3. Results and discussion

3.1. Morphological and structural characterization

To verify the successful synthesis of T-*X*U composites, XRD was performed to evaluate the as-synthesis product. From Fig. 1a, the main diffraction peaks of T-*X*U were observed at 2θ of 25.3°, 37.9°, and 48.1°, which can be attributed to (101), (004), and (200) crystal planes of anatase TiO_2 (JCPDS card no. 21-1272) respectively. XRD results confirmed the presence of TiO_2 in the as-synthesised T-*X*U. However, no obvious peaks of UiO-67 were observed in pattern of the composites, which results from the negligible doping amount of UiO-67. The morphology and microstructure of T-10%U after the solvothermal growth were tested by TEM images (Fig. 1c and d). It is obvious that T-10%U exhibits two morphologies containing thin nanosheet morphology and small octahedral nanocrystal. According to the high-resolution transmission electron microscope (HRTEM) images (Fig. 1e), the nanosheets of T-10%U show the lattice fringe with a pitch of 0.35 nm, which is in accordance with typical (101) plane of anatase TiO_2. Thus, it can be concluded that the thin nanosheet morphology is responding to TiO_2 and small octahedral nanocrystal is UiO-67, respectively. There, we indicate that the UiO-67 is a good growth matrix for TiO_2 particles. Furthermore, the FT-IR spectroscopy was used to confirm the chemical composition of T-10%U. Fig. 1b shows that UiO-67 and T-10%U exhibit similar FT-IR spectra. The wide peak centred at 3431 cm^{-1} can be attributed to stretching vibration of the hydroxyl group from BPDC. The peaks around 1606 cm^{-1} and 1592 cm^{-1} represent the C–O–Zr and vibrations of the benzene dicarboxylate skeleton, respectively. The distinct absorption peaks at 1409 cm^{-1} and 1530 cm^{-1} refer to vibrations of the stretching vibrations of the Zr–OH groups,[37,38] which confirms the doping of UiO-67. Besides, the peak of Zr–O stretching vibration at 768 cm^{-1}, 670 cm^{-1} are not obvious in T-10%U, which may be attributed to its replacement by a wide absorption peak of TiO_2 appearing at the range of 500–800 cm^{-1}.[31] From all observations mentioned above, it can be concluded that the T-10%U is effectively composited by UiO-67 and TiO_2.

The chemical composition and interfacial state of TiO_2, UiO-67 and T-10%U heterostructure were further investigated by XPS technique. As shown in Fig. 2a, the elements C, O, Ti and Zr exist in the XPS spectrum of T-10%U, implying that the T-10%U was composed by two phases. For T-10%U, the binding energies of Zr $3d_{3/2}$ and Zr $3d_{5/2}$ are responding to 184.4 eV and 182.2 eV (Fig. 2b). The Ti 2p also shows two peaks which can be assigned to the Ti $2p_{1/2}$ (464.4 eV) and Ti $2p_{3/2}$ (458.5 eV) in Fig. 2c. The characteristic peaks of O_{1s} at 531.5 eV,530.0 eV, 529.5 eV are responding to –COOH, –C═O and Zr–O/Ti–O, respectively (Fig. 2d). In Fig. 3e, the binding energy of C at 288.8 eV, 285.4 eV and 284.7 eV at 284.7 eV in T-10%U can be attributed to the

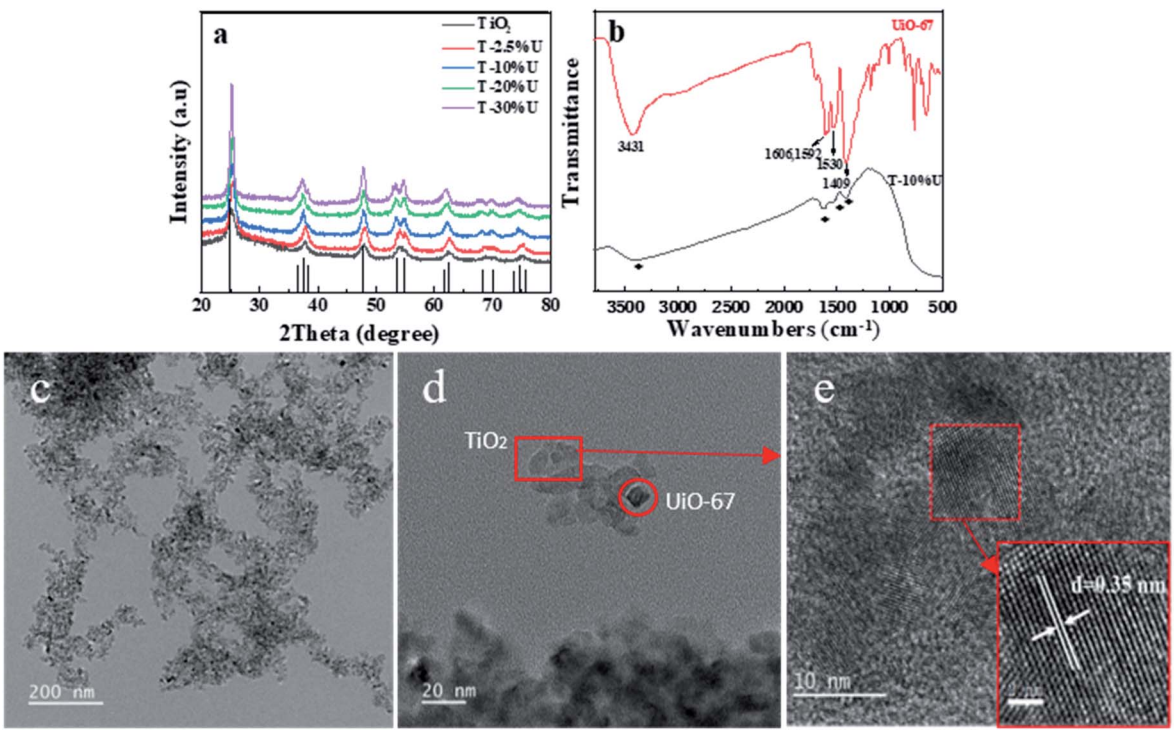

Fig. 1 XRD patterns for (a) T-*X*U (*X* = 2.5%, 10%, 20%, 30%), synthesized TiO_2 and simulated pattern for TiO_2. (b) FT-IR spectra of UiO-67 and T-10%U. (c)–(e) HRTEM images of T-10%U at different magnifications.

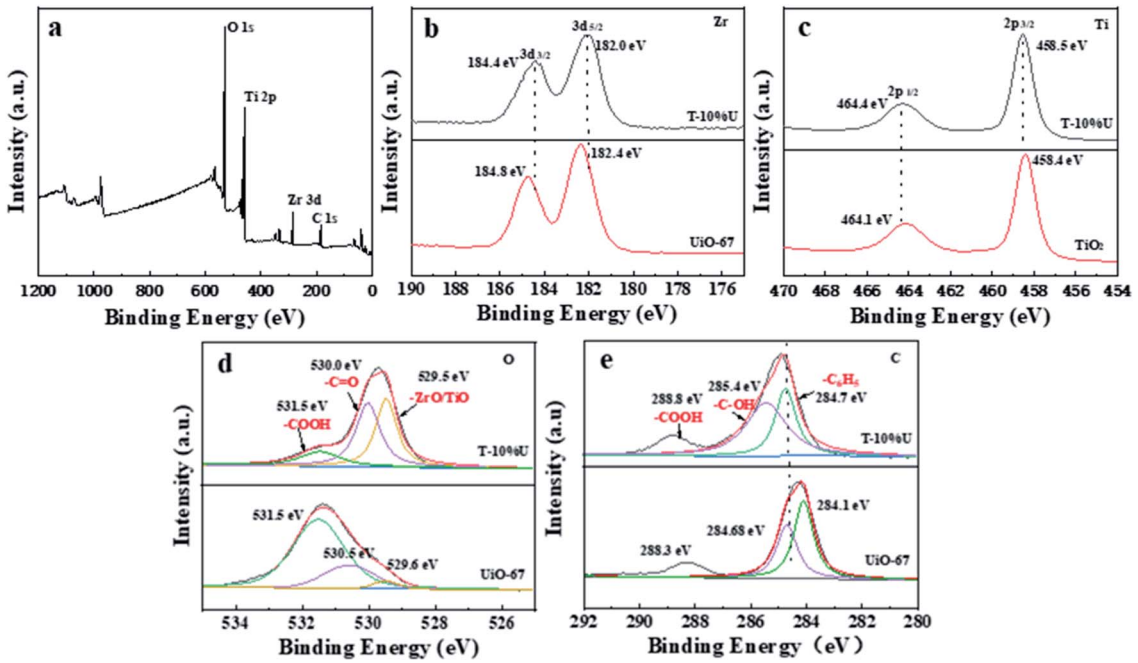

Fig. 2 (a) XPS survey spectra of T-10%U. (b) HR-XPS spectra of Zr 3d for T-10%U, UiO-67. (c) HR-XPS spectra of Ti 2p for T-10%U, TiO_2. (d) HR-XPS spectra of O 1s orbitals for T-10%U, UiO-67. (e) HR-XPS spectra of C in the T-10%U and UiO-67.

–COOH, –C–OH, $-C_6H_5$ groups, respectively. Compared with UiO-67, Fig. 2b and c shows that the peaks at binding energies of Zr $3d_{3/2}$ and Zr $3d_{5/2}$ in the T-10%U are lower than those in pure UiO-67, and the binding energies of the Ti $2p_{1/2}$ and Ti $2p_{3/2}$ orbitals in the T-10%U shifted upward in comparison with TiO_2, indicating the electrons transferred from TiO_2 to UiO-67 at the heterostructure interface. Besides that, the binding energy of C of T-10%U shifted higher in comparison to UiO-67 (284.1 eV, 285.4 eV, 288.8 eV) and the binding energy of O (530.0 eV) shifted lower than UiO-67 which demonstrated the

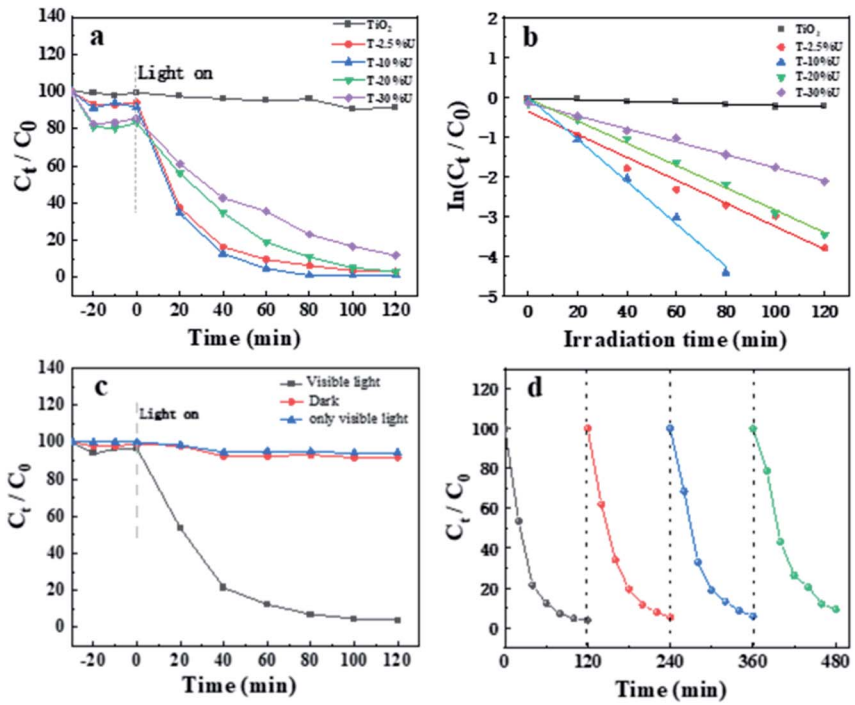

Fig. 3 (a) Photocatalytic degradation of AFB1 over as-prepared catalysts under visible light irradiation. (b) The corresponding plot of $\ln[C_t/C_0]$ *vs.* time for T-*X*U, TiO_2. (c) Photocatalytic degradation of AFB1 over T-10%U with/without visible light irradiation and photocatalytic degradation of AFB1 only visible light. (d) Cycling tests of the visible-light induced photodegradation of AFB1 over T-10%U.

chemical environment of TiO_2 is changed after doping the UiO-67. All these results indicate an intimate contact and strong interactions has been established between TiO_2 and UiO-67, which is beneficial to the photogenerated electron–hole pairs separation.

3.2. Photocatalytic performance

The photocatalytic performance of TiO_2 and T-*X*U were investigated by degradation of AFB1. Fig. 3a shows the degradation rate of AFB1 under visible light irradiation (λ > 420 nm). After the equilibrium of adsorption–desorption in dark condition for 30 min, the adsorption percentages on T-*X*U were higher than TiO_2, which could be owing to the large surface of UiO-67. The AFB1 degradation rate was followed the order: T-10%U > T-2.5%U > T-20%U > T-30%U > TiO_2. The optimized T-10%U almost completely degraded AFB1 within 80 min, and the removal efficiency was 98.8%, which was superior to the commercial P25, commercial TiO_2 and most of reported photocatalysts (Table S3 and Fig. S4b†).[39–41] The superior photocatalytic performance of T-*X*U composites compared with TiO_2 can be attributed to the heterostructure construction between TiO_2 and UiO-67, which plays a significant role in accelerating the photocatalytic process. Moreover, the plot of $\ln[C/C_0]$ as a function of the irradiation time was shown in Fig. 3b. According to the linear fit of $\ln[C/C_0] = -kt + b$, it is obvious that the photocatalysis process follows pseudo-first-order models and the value of k for T-10%U is the highest among the four samples (Table S2†), which agreed well with the photocatalytic behaviours shown in Fig. 3a. In addition, photocatalytic degradation over T-10%U with/without visible light irradiation and only with visible light was carried out to prove that the visible light and photocatalyst were necessary for degradation of AFB1 (Fig. 3c). For better application of photocatalyst, the stability and recyclability of catalysts were further evaluated. The degradation rate of AFB1 was 90.8% after 4 photocatalytic cycles which is in agreement with the XRD and IR data of T-10%U before and after 4 cycles (Fig. S6†), proving that the T-10%U composite is a stable catalyst (Fig. 3d).

3.3. Enhanced photocatalytic activity mechanism

To reveal the mechanism of enhanced photocatalytic activity, light absorption and charge separation were examined as principal factors.[6,42] As the UV-vis DRS pattern shown (Fig. 4a), the adsorption edges of TiO_2 and T-10%U was 407 nm and 434 nm (inset figure), indicating that T-10%U has higher visible light adsorption. We further evaluated the band gap energy of the samples according to Tauc curve: $(\alpha h\nu) = A(h\nu - E_g)^{n/2}$, where α, E_g, h, ν and A are the absorption coefficient, band gap energy, Planck's constant, optical frequency and constant, respectively.[43] The corresponding bandgaps of T-10%U, TiO_2 and UiO-67 are 2.21 eV, 3.18 eV, and 3.14 eV, respectively (Fig. 4a and b). These results confirmed T-10%U with the narrowing bandgap and better light absorption capacity, which is more easily for photogenerated electron–hole pairs to separate.

To further explain the improved photocatalytic performance of the TiO_2/UiO-67 heterostructure, a series of photoelectrochemical measurements were performed to access the distinction between TiO_2 and T-*X*U. As shown in Fig. 4c, it was clearly found that the fluorescence intensity of T-*X*U is lower than that of TiO_2, which proves that the photogenerated electron–hole pairs in T-*X*U have the highest separation efficiency. Meanwhile, a similar activity trend was observed in the transient photocurrent and EIS (Fig. 4d and e). Compared with UiO-67 and TiO_2, the T-10%U shows a higher light current information density and a smaller lowest arc radius. Based on the above discussion, the T-10%U shows higher photoelectric charge separation efficiency and better electrical conductivity, which is another important evidence of the increased photocatalytic activities in this study.

3.4. The photocatalysis mechanism

Here, in order to explain the interfacial state and electronic structure of the TiO_2/UiO-67 heterostructure, Mott–Schottky analyses were performed to certain the band potentials for TiO_2 and UiO-67 at the frequency of 1000 Hz. The slopes of all samples are positive in Mott–Schottky, indicating TiO_2 and UiO-67 are typical n-type semiconductor.[30,44] Besides that, the flat band position of TiO_2 and UiO-67 is corresponding to −0.50 V and −0.43 V *vs.* NHE, respectively (Fig. S8a and b†). The conduction band potential E_{CB} of n-type semiconductor is 0.2 V higher than the flat band potential.[30,45] Therefore, the E_{CB} of TiO_2 and UiO-67 are estimated to be −0.70 V and −0.63 V, respectively. According to the value of E_g and the formula of $E_g = E_{VB} - E_{CB}$, the corresponding bandgaps were estimated at 3.18 eV for TiO_2 and the corresponding bandgaps of UiO-67 is 3.14 eV. Based on the above results, the TiO_2/UiO-67 heterojunction are traditional type II heterojunction[21] and space charge regions are formed at the semiconductor interface, where photogenerated electrons and holes migrate in opposite directions (Fig. 5).

Furthermore, we carried out the free radical trapping tests of T-10%U heterostructure in order to demonstrate the active groups during the photoreaction. In this study, the different scavenger reagents including *t*-BuOH, EDTA and BQ as $^{\bullet}OH$, h^+ and $^{\bullet}O_2^-$ scavengers were used to identify the main active radicals during the photocatalytic reaction.[40,44,46] It is shown that the photocatalytic degradation efficiency of T-10%U composite decreased from 98.8% to 16.03%, 76.97% and 30.52% after EDTA, *t*-BuOH, BQ added under 2 h visible light illumination (Fig. 4f). The results indicated that $^{\bullet}O_2^-$, $^{\bullet}OH$ and h^+ were the main active groups during photocatalytic reaction. Thus, the T-*X*U generate photo-generated electrons and holes under the excitation of visible light, and then reacted with H_2O and dissolved oxygen in AFB1 aqueous solution to generate $^{\bullet}O_2^-$, h^+ and $^{\bullet}OH$. Furthermore, the main active species can oxidize AFB1 molecular to different small molecules.

According to the previous analysis, we proposed possible photocatalytic mechanism in following equations: (1) under visible light illumination, the electrons on the CB of T-10%U are excited and migrated to the VB, resulting in photoelectrons and cavities; (2) H_2O/OH^- reacted with h^+ at the VB of TiO_2 and produced $^{\bullet}OH$ due to potential of E_{VB} of TiO_2 is more positive than the potential energy of $H_2O/^{\bullet}OH$ (2.4 eV *vs.* NHE).[40] (3)

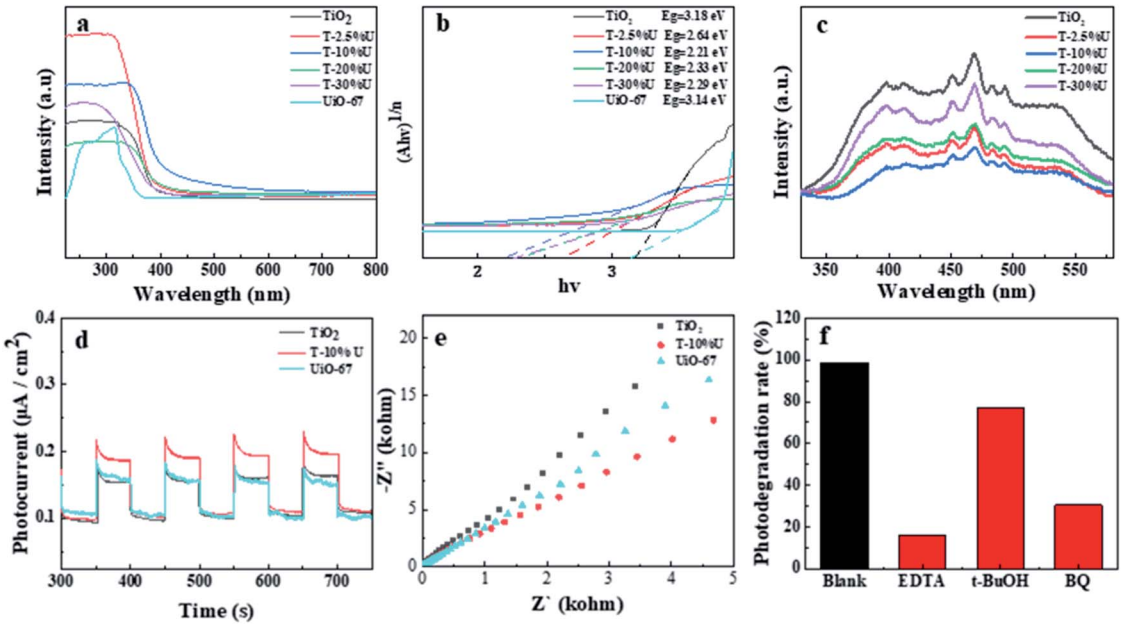

Fig. 4 (a) and (b) UV-vis DRS pattern and (c) PL spectra of T-*X*U and TiO_2. (d) EIS Nyquist plots and (e) photocurrent responses of T-10%U and TiO_2 under visible illumination. (f) Trapping measurements of the active species for degradation of AFB1.

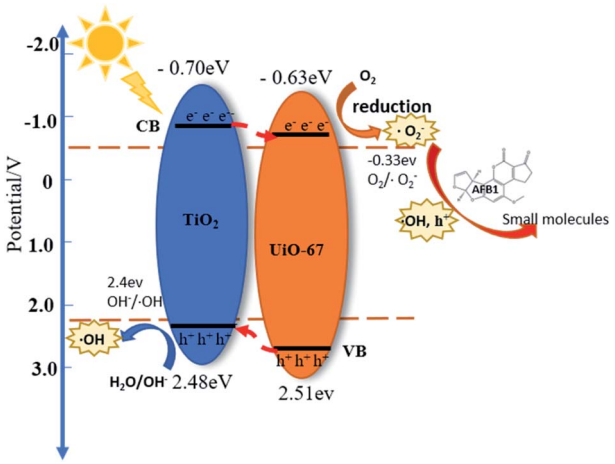

Fig. 5 Schematics of the mechanism of AFB1 degradation over the TiO_2/UiO-67 heterojunction.

Meanwhile, the CB potential of UiO-67 is more negative than the potential energy of $O_2/{}^{\bullet}O_2^-$ (−0.33 eV *vs.* NHE), then dissolved oxygen in water were reduced by photogenerated electrons to produce ${}^{\bullet}O_2^-$;[39] (4) and (5) a small number of ${}^{\bullet}O_2^-$ radicals and electrons were coupled with H^+ through multi-reaction to generate ·OH;[41] (6) the photo-generated holes and ·OH, ${}^{\bullet}O_2^-$ were main active groups for degrading AFB1, and they further reacted with AFB1 to form some small molecules.

$$TiO_2/UiO\text{-}67 + h\nu \rightarrow TiO_2(h^+) + UiO\text{-}67(e^-) \quad (1)$$

$$H_2O/(OH^-) + TiO_2(h^+) \rightarrow {}^{\bullet}OH \quad (2)$$

$$O_2 + UiO\text{-}67(e^-) \rightarrow {}^{\bullet}O_2^- \quad (3)$$

$${}^{\bullet}O_2^- + e^- + 2H_2O(H^+) \rightarrow H_2O_2 \quad (4)$$

$$H_2O_2 + e^- \rightarrow {}^{\bullet}OH + OH^- \quad (5)$$

$${}^{\bullet}O_2^- + h^+ + {}^{\bullet}OH + AFB1 \rightarrow \text{small molecules} \quad (6)$$

4. Conclusions

The *in situ* solvothermal method was adopted to fabricate TiO_2/UiO-67 heterostructure successfully. In this work, the T-10%U composite exhibits higher photocatalytic activity (98.9%) for AFB1 degradation than synthesised TiO_2, commercial TiO_2 and the commercial P25, and most of reported photocatalysts. In addition, T-10%U composite with excellent stability and photocatalysis activity after 4 cycles. The improved photocatalytic activity of TiO_2/UiO-67 can be attributed to two main factors. Firstly, the TiO_2/UiO-67 heterojunction which has matched energy band structures leads to efficient separation and transfer of photogenerated electron–hole pairs. Secondly, visible light response is improved after construction of TiO_2/UiO-67 heterostructure. The AFB1 degrading mechanism indicates that O_2^-, h^+ and ·OH are the main active species, which oxidized AFB1 during the photocatalysis process. This research of TiO_2/MOF based heterostructure photocatalyst may provide a novel perspective for toxin and organic pollutants degradation.

Conflicts of interest

There are no conflicts to declare.

Acknowledgements

The authors would like to thank the financial support and guidance provided by Professor Zenghe Li.

Notes and references

1 J. Li, J. Huang, Y. Jin, C. Wu, D. Shen, S. Zhang and R. Zhou, *J. Hazard. Mater.*, 2018, **359**, 382–387.
2 M. Loi, F. Fanelli, V. C. Liuzzi, A. F. Logrieco and G. Mule, *Toxins*, 2017, **9**, 111.
3 D. Conradt, M. A. Schatzle, J. Haas, C. A. Townsend and M. Muller, *J. Am. Chem. Soc.*, 2015, **137**, 10867–10869.
4 Y. Dai, K. Huang, B. Zhang, L. Zhu and W. Xu, *Food Chem. Toxicol.*, 2017, **109**, 683–689.
5 R. M. Elsanhoty, I. A. Al-Turki and M. F. Ramadan, *Water Sci. Technol.*, 2016, **74**, 625–638.
6 X. Yang, Z. Chen, W. Zhao, C. Liu, X. Qian, M. Zhang, G. Wei, E. Khan, Y. Hau Ng and Y. Sik Ok, *Chem. Eng. J.*, 2021, **405**, 126806.
7 Z. Long, Q. Li, T. Wei, G. Zhang and Z. Ren, *J. Hazard. Mater.*, 2020, **395**, 122599.
8 R. Kumar, P. Raizada, N. Verma, A. Hosseini-Bandegharaei, V. K. Thakur, Q. V. Le, V.-H. Nguyen, R. Selvasembian and P. Singh, *J. Cleaner Prod.*, 2021, **297**, 126617.
9 A. Kumar, P. Raizada, P. Singh, R. V. Saini, A. K. Saini and A. Hosseini-Bandegharaei, *Chem. Eng. J.*, 2020, **391**, 123496.
10 V. Hasija, P. Raizada, A. Sudhaik, K. Sharma, A. Kumar, P. Singh, S. B. Jonnalagadda and V. K. Thakur, *Applied Materials Today*, 2019, **15**, 494–524.
11 A. Sudhaik, P. Raizada, P. Shandilya, D.-Y. Jeong, J.-H. Lim and P. Singh, *J. Ind. Eng. Chem.*, 2018, **67**, 28–51.
12 S. Meephon, T. Rungrotmongkol, N. Kaiyawet, S. Puttamat and V. Pavarajarn, *Catal. Lett.*, 2018, **148**, 873–881.
13 Q. Guo, C. Zhou, Z. Ma and X. Yang, *Adv. Mater.*, 2019, **31**, 1901997.
14 K.-C. Lee and K.-H. Choo, *Chem. Eng. J.*, 2013, **231**, 227–235.
15 P. Raizada, V. Soni, A. Kumar, P. Singh, A. A. Parwaz Khan, A. M. Asiri, V. K. Thakur and V.-H. Nguyen, *Journal of Materiomics*, 2021, **7**, 388–418.
16 A. Kumar, P. Raizada, A. Hosseini-Bandegharaei, V. K. Thakur, V.-H. Nguyen and P. Singh, *J. Mater. Chem. A*, 2021, **9**, 111–153.
17 A. Sudhaik, P. Raizada, P. Singh, A. Hosseini-Bandegharaei, V. K. Thakur and V.-H. Nguyen, *J. Environ. Chem. Eng.*, 2020, **8**, 104483.
18 C. Zhao, Y. Li, H. Chu, X. Pan, L. Ling, P. Wang, H. Fu, C. C. Wang and Z. Wang, *J. Hazard. Mater.*, 2021, **419**, 126466.
19 Q. Liang, X. Liu, J. Wang, Y. Liu, Z. Liu, L. Tang, B. Shao, W. Zhang, S. Gong, M. Cheng, Q. He and C. Feng, *J. Hazard. Mater.*, 2021, **401**, 123355.
20 G. Li, B. Jiang, X. Li, Z. Lian, S. Xiao, J. Zhu, D. Zhang and H. Li, *ACS Appl. Mater. Interfaces*, 2013, **5**, 7190–7197.
21 J. Low, J. Yu, M. Jaroniec, S. Wageh and A. A. Al-Ghamdi, *Adv. Mater.*, 2017, **29**, 1601694.
22 L. Jiao, J. Y. R. Seow, W. S. Skinner, Z. U. Wang and H.-L. Jiang, *Mater. Today*, 2019, **27**, 43–68.
23 H. C. Zhou and S. Kitagawa, *Chem. Soc. Rev.*, 2014, **43**, 5415–5418.
24 V. Hasija, S. Patial, P. Raizada, A. Aslam Parwaz Khan, A. M. Asiri, Q. Van Le, V.-H. Nguyen and P. Singh, *Coord. Chem. Rev.*, 2022, **452**, 214298.
25 G. Yilmaz, S. B. Peh, D. Zhao and G. W. Ho, *Adv. Sci.*, 2019, **6**, 1901129.
26 Y. Shi, A.-F. Yang, C.-S. Cao and B. Zhao, *Coord. Chem. Rev.*, 2019, **390**, 50–75.
27 Y. Dou, J. Zhou, A. Zhou, J.-R. Li and Z. Nie, *J. Mater. Chem. A*, 2017, **5**, 19491–19498.
28 J. Chen, X. Zhang, X. Shi, F. Bi, Y. Yang and Y. Wang, *J. Colloid Interface Sci.*, 2020, **579**, 37–49.
29 B. Zhang, J. Zhang, X. Tan, D. Shao, J. Shi, L. Zheng, J. Zhang, G. Yang and B. Han, *ACS Appl. Mater. Interfaces*, 2018, **10**, 16418–16423.
30 J. Zhang, Z. Guo, Z. Yang, J. Wang, J. Xie, M. Fu and Y. Hu, *ChemCatChem*, 2020, **13**, 581–591.
31 C. Zhang, D. Guo, T. Shen, X. Hou, M. Zhu, S. Liu and Q. Hu, *Colloids Surf., A*, 2020, **589**, 124484.
32 X. Wang, W. Sun, Y. Tian, K. Dang, Q. Zhang, Z. Shen and S. Zhan, *Small*, 2021, **17**, 2100367.
33 A. Schaate, P. Roy, A. Godt, J. Lippke, F. Waltz, M. Wiebcke and P. Behrens, *Chemistry*, 2011, **17**, 6643–6651.
34 M. J. Katz, Z. J. Brown, Y. J. Colon, P. W. Siu, K. A. Scheidt, R. Q. Snurr, J. T. Hupp and O. K. Farha, *Chem. Commun.*, 2013, **49**, 9449–9451.
35 X. Yu, J. Huang, J. Zhao, S. Liu, D. Xiang, Y. Tang, J. Li, Q. Guo, X. Ma and J. Zhao, *Chem. Eng. J.*, 2021, **403**, 126359.
36 S. Li, B. Xue, J. Chen, Y. Liu, J. Zhang, H. Wang and J. Liu, *Sep. Purif. Technol.*, 2021, **254**, 117579.
37 Y. Han, X. He, W. Yang, X. Luo, Y. Yu, W. Tang, T. Yue and Z. Li, *Food Chem.*, 2021, **345**, 128839.
38 Q. Yang, J. Wang, X. Chen, W. Yang, H. Pei, N. Hu, Z. Li, Y. Suo, T. Li and J. Wang, *J. Mater. Chem. A*, 2018, **6**, 2184–2192.
39 J. Mao, P. Li, J. Wang, H. Wang, Q. Zhang, L. Zhang, H. Li, W. Zhang and T. Peng, *Appl. Catal., B*, 2019, **248**, 477–486.
40 J. Mao, Q. Zhang, P. Li, L. Zhang and W. Zhang, *Chem. Eng. J.*, 2018, **334**, 2568–2578.
41 J. Mao, L. Zhang, H. Wang, Q. Zhang, W. Zhang and P. Li, *Chem. Eng. J.*, 2018, **342**, 30–40.
42 L. Buzzetti, G. E. M. Crisenza and P. Melchiorre, *Angew. Chem., Int. Ed. Engl.*, 2019, **58**, 3730–3747.
43 X. Tang, T. Fan, C. Wang and H. Zhang, *Small*, 2021, **17**, 2005640.
44 X. Gao, S. Zhang, J. Liu, S. Xu and Z. Li, *RSC Adv.*, 2020, **10**, 40619–40624.
45 J. Zheng and Z. Lei, *Appl. Catal., B*, 2018, **237**, 1–8.
46 S. Sun, R. Zhao, Y. Xie and Y. Liu, *Food Control*, 2019, **100**, 183–188.